Acoustics and Performance Characteristics of an Ideally Twisted Rotor in Hover

Nicole A. Pettingill,* Nikolas S. Zawodny,† Christopher S. Thurman,‡ Leonard V. Lopes,§

NASA Langley Research Center, Hampton, VA, 23681

A series of experiments were conducted in an anechoic chamber to investigate the noise and performance of an ideally twisted rotor design, leading to validation of a low-fidelity aerodynamic performance and acoustic modeling tool chain. An "ideally twisted" rotor was designed in order to simplify the theoretical rotor inflow for a target thrust condition in hover. This rotor design was then fabricated using state-of-the-art rapid prototyping and tested in an anechoic chamber facility. Aerodynamic load and acoustic data were acquired across a range of rotation rates (RPM) and rotor collective settings in order to ascertain the accuracy of the low-fidelity modeling codes. Emphasis was placed on modeling of the broadband self-noise generated by the rotor system due to the fact that it was found to be a prominent contributor to the overall rotor system noise.

Nomenclature

English

Rotor collective angle, deg. A_0

Chord length, m c

Thrust coefficient, $\frac{T}{\rho\pi\Omega^2R^4}$

 $M_{\rm tip}$ Tip Mach number

Number of rotor blades

Torque, $N \cdot m$ Q

Spanwise location from hub, m

RBlade radius, m

Strouhal number relative to chord, $\frac{f * c}{U_{tin}}$ St

TThrust, N

 $U_{\rm tip}$ Tip speed, m/s

Greek

Local aerodynamic angle of attack, deg.

Local induced angle, deg. ϕ

Rotor solidity, $\frac{N_b * c}{\pi R}$ σ

Observer angle, deg.

Θ Blade pitch angle, deg.

Blade tip pitch angle, deg.

Rotation rate, RPM

Subscript

Corrected rotation rate (for sea level, standard day conditions)

^{*}Research Aerospace Engineer, Aeroacoustics Branch, AIAA Member; nicole.a.pettingill@nasa.gov

[†]Research Aerospace Engineer, Aeroacoustics Branch, AIAA Member; nikolas.s.zawodny@nasa.gov

[‡]Graduate Research Assistant, Aeroacoustics Branch, AIAA Member; christopher.thurman@nasa.gov

[§]Senior Research Aerospace Engineer, Aeroacoustics Branch, AIAA Member; leonard.v.lopes@nasa.gov

I. Introduction

Characterizing noise sources of small rotor blades is important as they are applicable to small UAS, and potentially to larger, UAM vehicle platforms. Furthermore, assessment of the available low-fidelity acoustic tools is important as they will be used to predict noise sources and influence the vehicle design process. This paper will serve in further validation of semiempirical noise prediction tools. A set of hover chamber experiments and corresponding predictions of an ideally twisted rotor will be discussed in this paper. While hover tests for rotors of these scales have been done, they have normally been done with commercial off the shelf (COTS) rotors. With these COTS rotors, it is not always possible to know the exact geometric properties or the complexity of the inflow. A rotor with an ideal twist distribution theoretically has uniform inflow, which may be simpler to predict using low-fidelity tools. The predictions of this abstract will focus on harmonic content and broadband self-noise; however, the final paper will discuss additional noise sources that may have been present in the experiment. The experimental work and predictions in this paper have helped with understanding the current broadband noise prediction method and its limitations. This, in turn, has influenced the development of the broadband noise prediction module in the ANOPP2¹ design suite. The toolset used for this abstract is similar to the broadband prediction methodology that has been employed in previously published predictions of small rotors, such as in Ref. 2. While broadband noise predictions in this abstract are presented using a semiempirical tool called Broadband Acoustic Rotor Codes (BARC), the final paper will present these predictions using the improved tool ANOPP2 Self Noise Internal Functional Module (ASNIFM).

This abstract will describe the technical approach of this study by introducing the rotor design method, the process used to manufacture the blades, the experiment and facility setup, and finally the low-fidelity noise prediction tools. Following this, preliminary results will show the progress made for the paper. These results will include performance measurements and processed acoustic data obtained in the hover chamber tests. In addition to this, experiments will be compared to initial tonal and broadband noise predictions. Finally, the abstract will conclude with a summary of future work and results that will be presented in the final paper.

II. Technical Approach

A. Rotor Design

The design parameters and conditions for the rotor in this study are summarized in Table 1. Blade element momentum theory (BEMT) with an ideal twist distribution was used to design the rotor. This method, described in Ref. 3, defines a rotor, which experiences uniform inflow, and thus minimum induced power in hover. An ideally twisted rotor with a constant chord is defined by the following blade pitch distribution:

$$\Theta(r/R) = \frac{\Theta_{\text{tip}}}{r/R},\tag{1}$$

and the local angle of attack and inflow angles are defined as:

$$\alpha(r/R) = \frac{\alpha_{\text{tip}}}{r/R},\tag{2}$$

$$\phi(r/R) = \Theta(r/R) - \alpha(r/R). \tag{3}$$

Table 1. Ideally twisted rotor design parameters.

	Parameter	Value
Geometry	R (m)	0.1588
	c/R	0.20
	Θ_{tip} (°)	6.9
	N_b	4
	σ	0.255
Operating	C_T	0.0137
Condition	$M_{ m tip}$	0.27
	Ω_c (RPM)	5500

The 4-bladed rotor was sized to a radius of R=0.1588 m. Dimensionally speaking, the rotor was designed to generate 11.12 N (2.5 lbs.) of thrust at a rotational speed of $\Omega_c=5500$ RPM. The distribution of Θ , α and ϕ along the span can be seen in Fig. 1. The nominal tip angles were a blade pitch of 6.9 degrees, induced angle of 4.7 degrees, and angle of attack of 2.1 degrees. The resulting thrust coefficient was $C_T=0.0137$, with a tip Mach number of $M_{\rm tip}=0.27$.

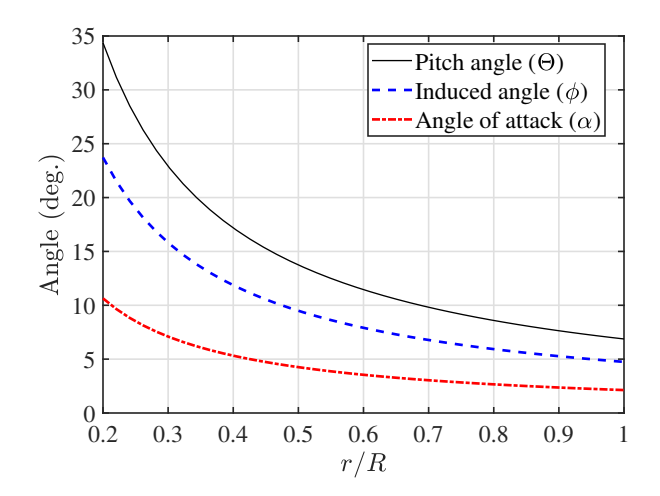


Figure 1. Spanwise angle distributions for designed ideally twisted rotor.

B. Blade Manufacturing

The rotor blades were printed in house because several printing iterations were expected due to the tall and thin structure of the rotor blades. The blades were manufactured at the NASA Langley Larkworks MakerSpace using a Markforged X7 3D printer. This printer has a build volume of 330 mm x 270 mm x 200 mm, a minimum possible layer height of 50 μ m and produces fiber-reinforced plastic parts. The blades tested in this study were printed out of carbon fiber-reinforced onyx plastic. Layers of the blades were printed in the radial direction. The blades were also printed with the blade standing from the leading edge. This layering technique resulted in a smooth airfoil definition in the chordwise direction. The blades were found to be very challenging to print due to a combination of the blade orientation during layering as well as the fact that only one blade could be printed at a time. As Fig. 2(a) shows, the blades were printed with mixed success. However, the blades that did print successfully were of excellent overall build quality and surface finish. The blade roots were designed to mate with a COTS hub made by varioPROP, which is a small-scale ground adjustable variable pitch propeller hub (see Figs. 2(b) and 2(c)). Using this hub it was possible to manually adjust the pitch of all 4 blades simultaneously.



(a) Blade printing iterations



(b) varioPROP hub

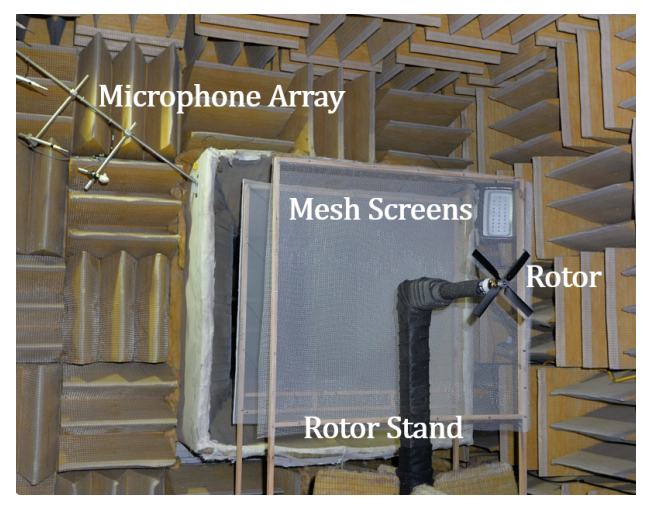


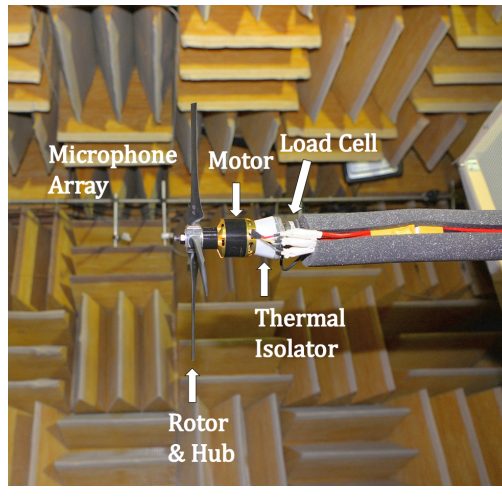
(c) Blade root design

Figure 2. Rotor blade manufacturing.

C. Experimental Setup

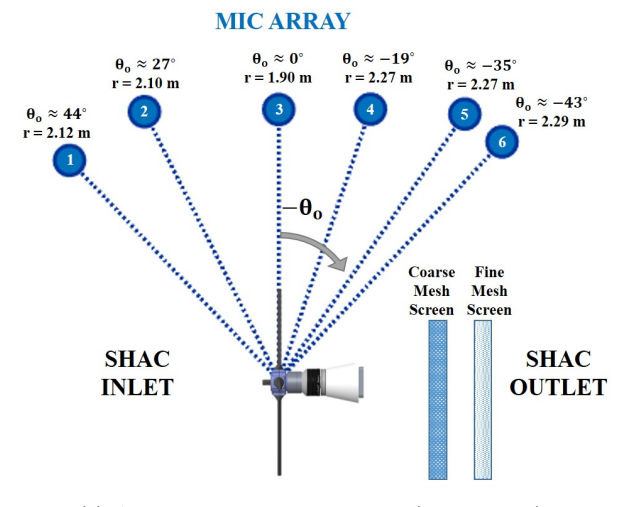
The experiment was conducted in the the Small Hover Anechoic Chamber (SHAC), a facility at the NASA Langley Research Center. Photos of the setup are shown in Fig. 3. The SHAC is acoustically treated down to 250 Hz and has dimensions of 3.87 x 2.56 x 3.26 m from wedge tip to wedge tip. This facility has been found in recent studies to be suitable for measuring the aerodynamic loads and acoustics of small rotors in static conditions when proper precautions are taken to address and mitigate the effects of flow recirculation (Ref. 4,5). Two mesh screens are placed in the chamber to reduce recirculation effects, as seen in the schematic in Fig. 3(c). More details of recirculation, the mesh setup, and the effective mitigation will discussed in the final paper. A Bruel & Kjaer (B&K) LAN-XI DAQ and BK Connect software system were used for for data acquisition. Six B&K Type 4939 free-field microphones are located in the upper corner of the SHAC, and span a range of +43.5° above the plane of the rotor to -43.1° below the plane of the rotor. These microphones are located about 12 rotor radii away from the rotor, which is in the far-field. A laser sensor tachometer located directly below the rotor was used to monitor the rotational rate of the rotor, and a 6-component AI-IA mini40 multiaxis load cell was used to measure the aerodynamic forces. The rotor was powered using a Scorpion 4020 DC brushless motor and a Castle Creations Edge 50 electronic speed controller.





(a) Testing setup in SHAC facility

(b) Mounted rotor, motor and load cell



(c) Acoustic measurement layout (not to scale)

Figure 3. SHAC facility and acoustic measurement configuration.

The test cases were divided into two primary parameter sweeps: a rotor rotation rate sweep and a rotor collective sweep. A summary of the testing conditions is provided in Table 2. The sweep of rotor rotation rates were acquired first to establish the target design operating condition, and these were done at the designed blade pitch of $\Theta_{\rm tip} \approx 6.9^{\circ}$. Following this, the root pitch was adjusted with the varioPROP hub to collectives of $A_0 \approx \pm 3^{\circ}$.

Table 2. Experimental testing conditions.

Parameter Sweep	Ω (RPM)	Θ _{tip} (°)
Rotation Rate (Ω)	$3000 \Rightarrow 6000^{a \ b}$	6.9
Rotor Collective (A_0)	5500^{a}	3.9, 6.9, 9.9

^aValues are approximate.

D. Low-Fidelity Prediction Tools

Several low-fidelity rotor performance and acoustic prediction tools are utilized in this study. The first two are part of the NASA Aircraft NOise Prediction Program (ANOPP), and are called the Propeller Analysis System (PAS)⁶ and the Rotorcraft System Noise Prediction System (ROTONET).⁷ These codes utilize BEMT to predict the aerodynamic loads on respective propellers and rotors.

In this study, PAS is utilized to predict the tonal noise characteristics of the ideally twisted rotor due to the fact that it has a more accurate acoustic solver that accounts for the full pressure distribution on the blade surface, while the current implementation of ROTONET utilizes a compact chord assumption. The ROTONET performance module assumes a fully articulated rotor with rigid blades and a simple uniform inflow model. ROTONET is specifically utilized to compute the inflow characteristics for the rotor in hover conditions, which is a condition that PAS cannot accurately model. An inflow velocity is required as an input into PAS and therefore cannot truly represent a hover condition. However, it has been found that a reasonably accurate prediction of a hover condition can be achieved with only a modest freestream velocity condition.

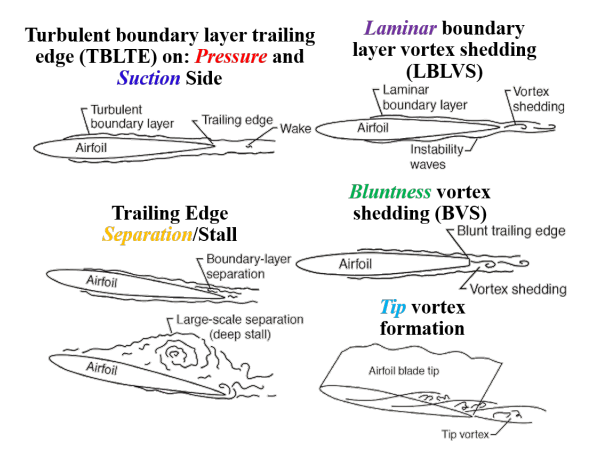


Figure 4. Self-noise mechanisms predicted by BARC. For more information on these noise sources, please see Refs. 2,9–11.

Broadband rotor self-noise predictions are currently performed using the Broadband Acoustic Rotor Codes (BARC) suite.^{2,9-11} This suite incorporates the semiempirical airfoil self-noise prediction routines of Ref. 10 into a rotating reference frame, given the appropriate aerodynamic conditions of discrete blade elements. ROTONET uses rotor definitions and flight conditions such as thrust, rotor angle, rotor speed, advance ratio and trim conditions as inputs in order to calculate inflow conditions for BARC. The self-noise prediction method uses empirical boundary layer data obtained by physically tripping and untripping a NACA0012 airfoil to define the boundary layer parameters. So BARC also requires a "tripped" or "untripped" boundary layer definition as an input. The self-noise mechanisms that will be predicted and discussed in this abstract are displayed in Fig. 4.

^bTested in approximate increments of 500 RPM.

III. Preliminary Results

This section will present preliminary results of both performance and acoustic test data. For the purposes of this abstract, presented acoustic spectra will correspond to an observer located -35° below the plane of the rotor (Microphone 5). The final paper will include additional test cases, comparisons to predictions and a more thorough analysis of the noise characteristics of this rotor.

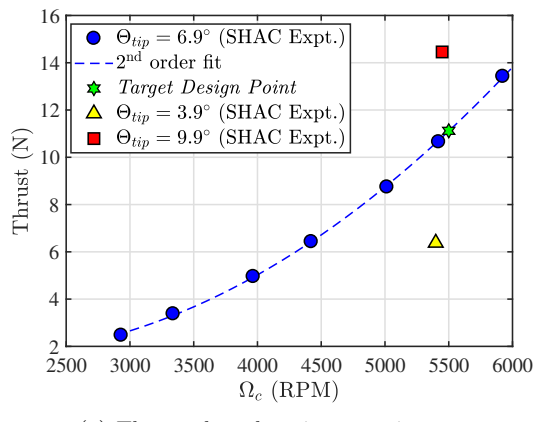
A. Performance Measurements

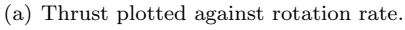
As described in the Experimental Setup section, a sweep of rotation rate conditions was performed for the design blade pitch of $\Theta_{\rm tip}=6.9^{\circ}$. Following this, the collective was adjusted so that the blade pitch at the tip was $\pm 3^{\circ}$ from the baseline condition (resulting in a near constant tip speed of about $M_{\rm tip}\approx 0.26$). Table 3 lists the measured performance values for these cases as well as the resulting thrust coefficients $C_T=T/(\rho\pi\Omega^2R^4)$ and tip Mach numbers $M_{\rm tip}$.

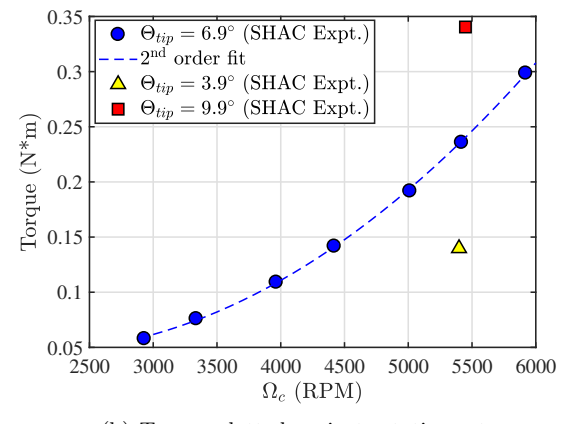
Pitch	Ω_{mech}	Thrust	${ m M_{tip}}$	C_{T}
6.9	5989	13.42	0.2893	0.0141
6.9	5480	10.67	0.2648	0.0133
6.9	5070	8.74	0.2449	0.0128
6.9	4470	6.43	0.2159	0.0121
6.9	4010	4.96	0.1937	0.0116
6.9	3375	3.38	0.1630	0.0112
6.9	2963	2.47	0.1431	0.0106
3.9	5465	6.38	0.2638	0.0080
6.9	5480	10.67	0.2648	0.0133
99	5514	14 46	0.2633	0.0179

Table 3. Performance of ideally twisted rotors in SHAC.

Thrust is plotted against rotation rate (corrected for standard day conditions) in Fig. 5(a). A second-order fit was applied to the rotation rate sweep, and the designed target thrust of 11.12 N fell on the line, indicating the ideal rotor is performing as predicted. The torque was also plotted against rotational rate in Fig. 5(b) and also followed a second-order curve fit. The two pitch collective cases are also plotted on both figures, to show they were targeted at the baseline rotation rate of $\Omega_c \approx 5400$ RPM.







(b) Torque plotted against rotation rate.

Figure 5. Thrust and torque are plotted against corrected rotation rate. The experimental data for both the rotation rate sweep (blue circles) and additional collective cases (red square and yellow triangle) are plotted in these figures.

B. Acoustic Data Processing

The following steps were taken to extract the stochastic, broadband content from the raw data (for additional information on the data processing techniques, see Ref. 12). First, the narrowband acoustic spectra were computed by using a fast Fourier Transform (FFT) of raw data treated as random data sets. This raw spectrum is plotted in Figure 6(a). Second, to separate the periodic and random components, the mean rotor revolution time history was computed. This was then subtracted from the time record to retain random noise components. An FFT was used to compute the periodic and broadband spectra from these mean and residual time series, and both spectra are plotted in Fig. 6(b). Finally, remaining peaks left in the residual signal were removed to more clearly see the broadband component. This "peak-removed" spectrum can be seen in black in Fig. 6(c). This final resulting spectrum is used for comparison with predictions; though it should be noted that the peak removal technique may not always be entirely effective, as it sometimes removes broadband noise content.

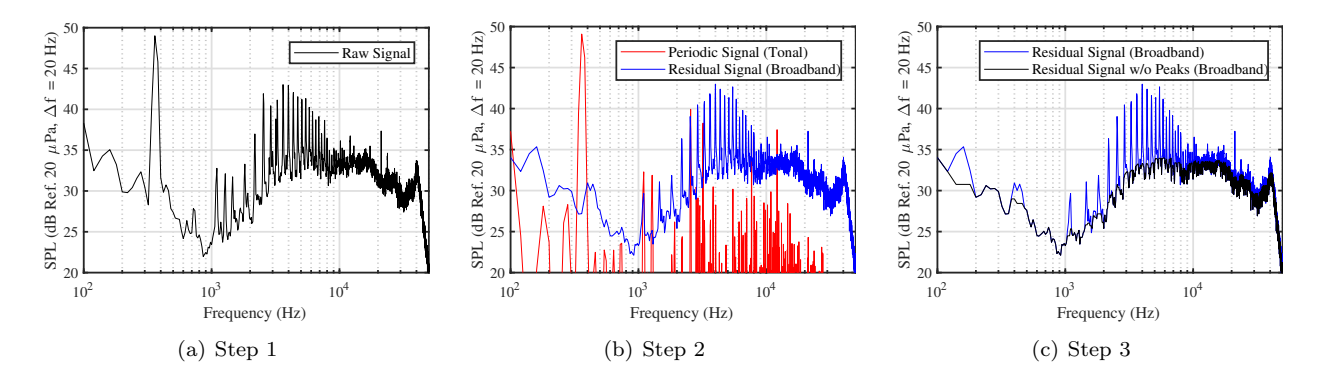


Figure 6. Processing steps for isolation of periodic and broadband noise contributions.

C. Experimental Broadband Noise Trends

1. Rotational Rate Sweep

To understand how broadband noise trends with thrust, Fig. 7 shows processed broadband noise for all seven rotational rate cases at $\Theta_{\rm tip}=6.9^{\circ}$. To clearly see the differences in thrust conditions, the broadband noise is presented with peaks removed. The increase in high frequency content between 50 kHz and 60 kHz present in the lower RPM cases is not a physical mechanism, but the result of limitations in the data acquisition of the microphone signal. Additionally, motor noise located between 21 kHz \leq f \leq 26 kHz is present in the data for lower RPM conditions. The noise below about 1 kHz is believed to be due to disturbances near the microphone.

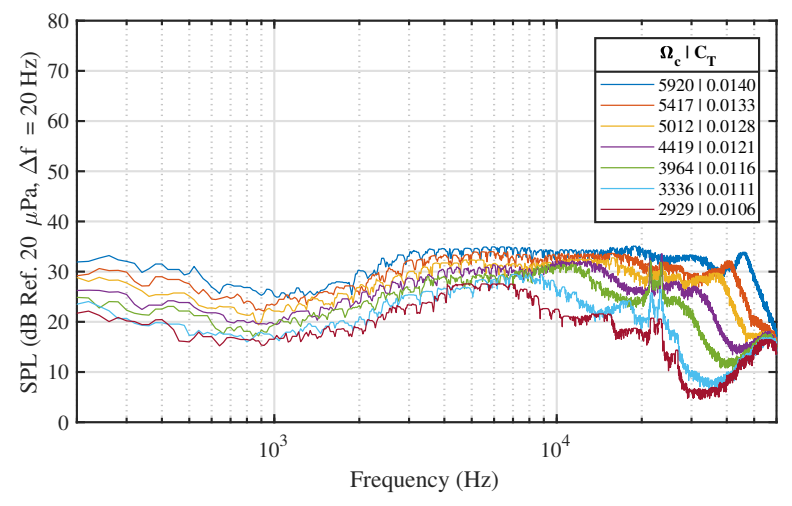
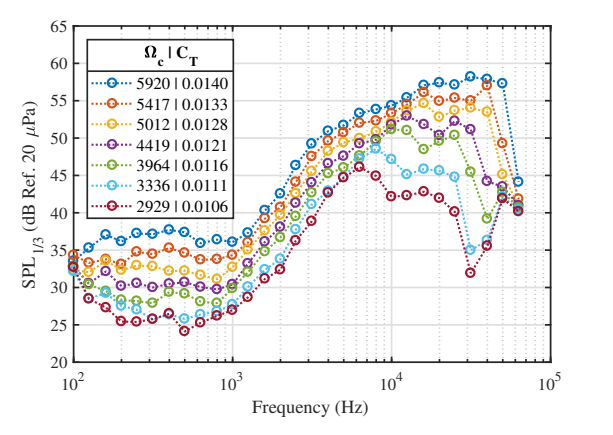
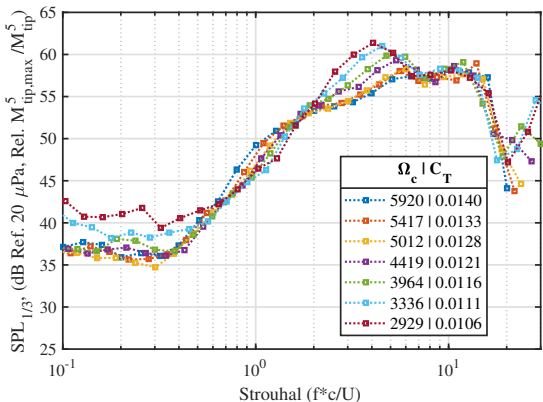


Figure 7. Peak-removed broadband noise spectra for the set of rotational rate sweep experiments at $\Theta_{\rm tip} = 6.9^{\circ}$.

It is believed that different noise sources are more prominent with different rotation rates. The highest RPM case has broadband noise spread over a larger range of of frequencies, with the exception of a high frequency "hump" that occurs at around 46 kHz. This is characteristic of bluntness vortex shedding (BVS), the self-noise mechanism resulting from vortices forming at the trailing edge and shedding into the airfoil's wake. This noise source is present in all the spectra, though diminished at the lowest rotational rate conditions. The noise at the lower rotational rates is confined to a smaller frequency range, as can be seen for the 2929 RPM case between $1 \text{kHz} \leq f \leq 10 \text{kHz}$. The transition from lower frequency noise sources to higher frequency noise sources is more defined for the lower rotation rate cases. It could be the case that below 4419 RPM the boundary layer is transitioning differently than at the higher rotation rates. To understand this better, the experimental data must be looked at further with spectral scaling.

Both dimensional and nondimensional trends of the broadband noise are presented in Fig. 8 for the seven rotational rate cases. The peak-removed broadband spectra for the various thrust conditions are presented as one-third octave spectra (SPL_{1/3}) in Fig. 8(a). The data were then nondimensionalized using the Strouhal number $St = f * c/U_{\infty}$ and tip Mach number M_{tip}^5 of the highest rotational rate case (5920 RPM). The results of scaling can be seen in Fig. 8(b). This scaling collapses the data along some of the frequencies, but it can be seen that for a Strouhal number range of $0.1 \le St \le 0.4$ and $2 \le St \le 5$, there is broadband noise that does not scale as initially expected. A possible cause for the lack of collapse at the higher St range could be laminar to turbulent boundary layer transition correlated with rotor speeds.





- (a) Dimensional spectra for various rotational rates.
- (b) Nondimensional spectra for various rotational rates.

Figure 8. Processed broadband spectra for a range of rotation rate conditions.

2. Pitch Sweep

Figure 9 shows the spectra for the different blade pitch conditions of $\Theta_{\rm tip}=3.9^\circ$, 6.9° and 9.9°. A few observations can be made when comparing collective conditions to the baseline case (pictured in red in the figure). First, there is additional broadband noise present for both collective conditions, between the frequencies of 12 kHz \leq f \leq 35 kHz. For the lower collective case pictured in blue, this additional noise occurs at 20 kHz \leq f \leq 35 kHz, but for the higher collective case pictured in black, this additional noise occurs at the lower frequencies of 12 kHz \leq f \leq 23 kHz. The spectral peaks at around 16 kHz and 19 kHz are indicative of laminar boundary layer vortex shedding (LBLVS), and are present in both comparative pitch collective cases. The additional noise at the 12 kHz \leq f \leq 23kHz range indicates more pressure side turbulent boundary layer trailing edge (pressure TBLTE) noise is present especially in the higher pitch collective case. Finally, at the highest frequencies, there is bluntness vortex shedding present for all pitch angles, though this mechanism is highest for the $\Theta_{\rm tip}=9.9^\circ$ case.

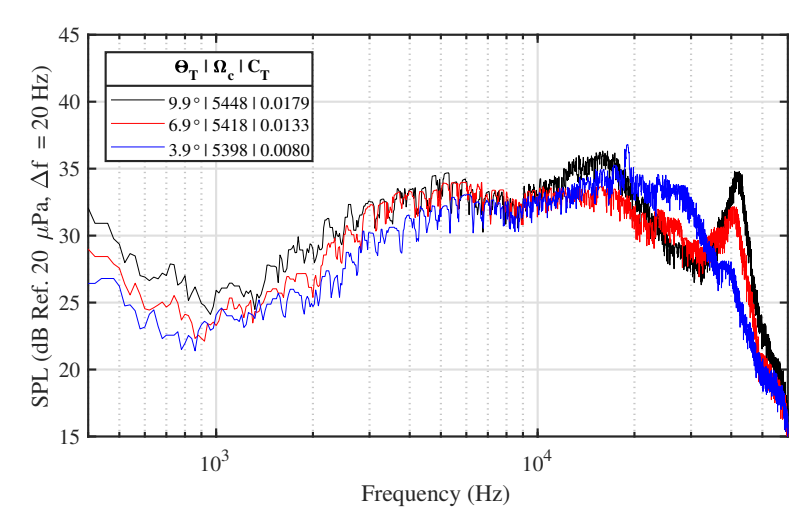


Figure 9. Peak-removed broadband noise spectra for the set of collective sweep experiments at $M_{\rm tip} \approx 0.26$.

D. Low-Fidelity Predictions

1. Tonal Noise Predictions

PAS is used initially to perform a tonal noise prediction of the ideally twisted rotor at the target design operating condition. Fig. 10(a) shows the predicted blade passage frequency (BPF) directivity for a range of observer elevation angles (see Fig. 3(c) for angle convention). Note that the data in this figure are normalized to a common radius of 1.90 m using spherical spreading. As Fig. 10(a) shows, the BPF directivity is seen to be thickness noise dominant across the entire range of computed observers. This is because of the relatively large rotor solidity and blade count, which reduces the aerodynamic loading per blade. As a result of this, it is expected that operating the rotor at different collectives for a fixed rotation rate would yield very similar noise levels. This is confirmed in Fig. 10(b), which shows commonality in directivity trends between the PAS predictions and SHAC measurements. The experiments show a maximum difference in levels between the lowest and highest blade pitch settings of 2.5 dB, which is very small compared to the considerable difference in thrust generated by the rotor at the different respective blade pitch settings (see Fig. 5(a)). These results provide further confidence in the low-fidelity blade design and modeling process.

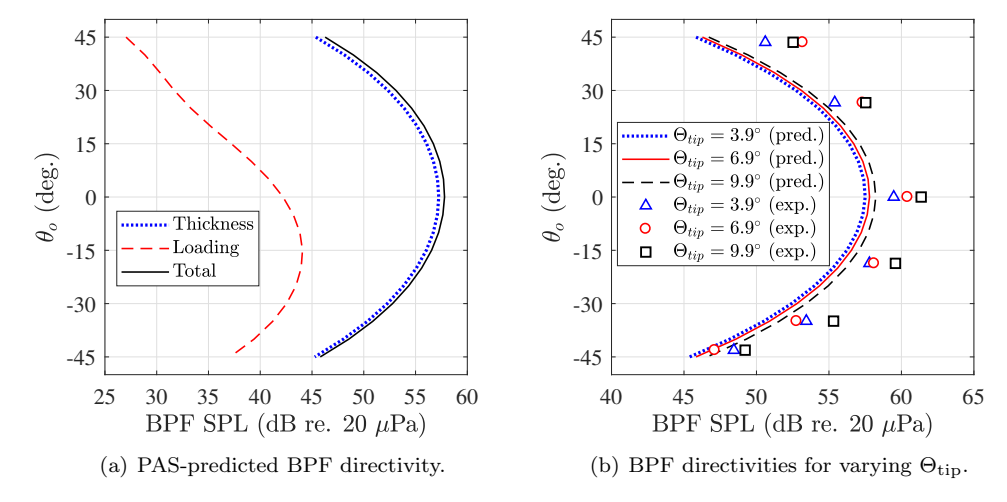
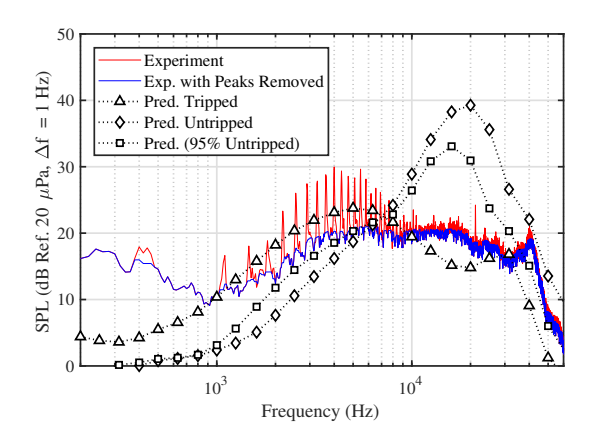
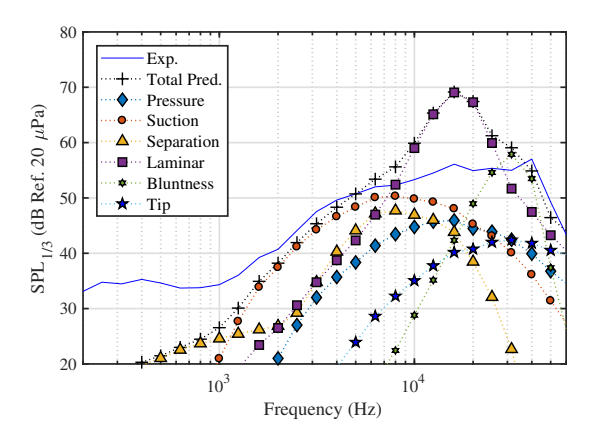


Figure 10. Acoustic directivity predictions and measurements of rotor BPF: (a) noise contribution predictions using PAS at target operating condition ($\Theta_{\rm tip}=6.9^{\circ}$), (b) comparison between PAS predictions and experimental SHAC measurements for different blade collective settings.

2. Broadband Noise Predictions

As described earlier, low-fidelity self-noise predictions have been made using ROTONET and BARC. The self-noise predictions are highly sensitive to the defined boundary layer condition. Figure 11(a) shows a comparison of the experimental baseline case to three different BARC predictions using three different boundary layer settings. Even though the rotor is physically smooth, an untripped-boundary layer setting does not capture the separation and suction noise that occurs between 1 kHz \leq f \leq 5 kHz. Broadband noise at this frequency does trend better with a tripped boundary layer condition, but the content between 10 kHz and 30 kHz behaves as LBLVS (as shown by the spectral scaling trends of the experiment). So, it was attempted to partially trip the last 5% portion of the blade, and the initial physical justification for this decision is that this portion of the blade may be experiencing a tip vortex that is impinging inboard, creating a boundary layer that behaves tripped for a certain distance inboard. It is noted that in Fig. 11(a), the 95% untripped prediction is overpredicting the LBLVS contribution. In the final paper, additional limiting of the laminar boundary layer mechanism by a parameter such as Reynolds number will be investigated. Additionally, high-fidelity simulations were performed in an accompanying paper, ¹³ which indicate tip vortex spillage acting on approximately 5% of the blade span, further confirming a partially tripped condition. Using this partially tripped prediction, the various self-noise mechanisms, as predicted by BARC, are broken down in Fig. 11(b). These spectra are presented in one-third octave bands to better distinguish the noise sources.





- (a) Effect of boundary layer settings on predictions.
- (b) Self-noise breakdown for the 95% untripped prediction.

Figure 11. Self-noise predictions for the baseline experimental case ($\Theta_{tip} \approx 6.9, \Omega_c \approx 5420$).

IV. Summary and Plans for Full Paper

The work presented in this abstract introduced the experimental data set that will be presented in the final paper. The 3-D printed ideally twisted rotor matched performance expectations when tested in the SHAC, and acoustic trends were identified for the rotational sweep and collective conditions. The low-fidelity predictions were introduced briefly, as this abstract focuses more on introducing these experimental results and initial conclusions.

Brief discussions of the self-noise mechanisms that may be present in these experiments were presented in this abstract, by mentioning LBLVS, BVS and pressure TBLTE noise. Additional self-noise sources will be discussed in the final paper. At this time, it is believed that LBLVS is present for this ideally twisted rotor at all rotational rates, but more prominent at the lower tip speeds. By scaling the Strouhal number based on the rotor chord and tip Mach number, it was possible to see the frequency ranges where broadband noise is not scaling with rotation rate. Future scaling will use a length scale associated with the boundary layer rather than the rotor geometry.

Though there are currently only three cases representing a pitch sweep, the experimental trends were introduced in this abstract. It is suspected that varying collective pitch significantly changes the noise sources and inflow conditions. To investigate this further, additional pitch collective experiments are planned, as well as the use of an aerodynamic modeling tool with nonuniform inflow modeling options such as CAMRAD II (Comprehensive Analytical Model of Rotorcraft Aerodynamics and Dynamics¹⁴). Finally, if time permits, an experimental flow field survey may provide insight into the nonuniform inflow conditions that may be

occurring at the $A_0 = \pm 3^{\circ}$ test conditions. It is suspected that additional broadband noise mechanisms may be present at certain operating conditions such as blade wake interaction and turbulence ingestion. The results of an accompanying paper¹³ will investigate these noise sources with a lattice-Boltzmann method solver.

Initial low-fidelity predictions are capable of reasonably predicting the tonal and broadband noise trends of this tested rotor. As an example for the purposes of this abstract, only one experimental case was compared to BARC predictions. However, the final paper will include predictions for the performance sweeps in order to see how well the broadband noise predictions trend with different performance conditions.

In the full publication, employment of the broadband noise prediction methodology will be improved using a more physical basis. This should allow for a more robust implementation that will account for specific broadband noise generation mechanisms such as boundary layer transition along the blade as well as secondary effects due to tip vortex generation. A coarse radial grid was used for the initial predictions shown in this abstract to quickly identify trends caused by different operating conditions; however, it is vital to refine the grid for future simulations. Certain noise generation mechanisms are sensitive to boundary layer conditions that change along the span of the blade and the current resolution may slightly mispredict these boundary layer conditions. It is anticipated that a finer grid, in conjunction with a modified implementation of the broadband noise prediction methodology, will produce more accurate results. For the final paper, semiempirical predictions will be presented using the ANOPP2 Self Noise Internal Functional Module (AS-NIFM), which can be used with the rest of the ANOPP2 suite to characterize and predict the noise impact of full vehicle designs.

Acknowledgments

The authors thank the NASA Revolutionary Vertical Lift Technology (RVLT) project and the NASA Langley Center Innovation Fund of Internal Research and Development (CF-IRAD) for funding this work. The authors thank Siena Whiteside who led the effort of the Aeronautics Systems Analysis Branch in design and printing of the blades used in this experiment. Beau Pollard designed the 3-D blades, and Shali Subramanian aided in both manufacturing and testing the blades in the SHAC. Finally, the LSAWT team (John Swartzbaugh, Stan Mason, Jeff Collins, Bryan Lamb and Mick Hodgins) helped with testing in the SHAC.

References

- ¹Lopes, L. V. and Burley, C., ANOPP2 User's Manual: Version 1.2, Hampton, VA, NASA/TM-2016-219342.
- ²Pettingill, N. A. and Zawodny, N. S., "Identification and Prediction of Broadband Noise for a Small Quadcopter," VFS Forum 75, 2019.
- ³Leishman, J. G., *Principles of Helicopter Aerodynamics*, chap. 3.3: Blade Element Momentum Theory (BEMT), Cambridge University Press, 2nd ed., 2002, pp. 87–113.
- ⁴Whiteside, S. K. S., Zawodny, N. S., Fei, X., Pettingill, N. A., Patterson, M. D., and Rothhaar, P. M., "An Exploration of the Performance and Acoustic Characteristics of UAV-Scale Stacked Rotor Configurations," *AIAA SciTech Forum*, No. January, 2019, pp. 1–20.
- ⁵Stephenson, J. H., Weitsman, D., and Zawodny, N. S., "Effects of flow recirculation on unmanned aircraft system (UAS) acoustic measurements in closed anechoic chambers," *The Journal of the Acoustical Society of America*, Vol. 145, No. 3, 2019, pp. 1153–1155.
- ⁶Nguyen, L. C. and Kelly, J. J., A Users Guide for the NASA ANOPP Propeller Analysis System, Hampton, VA, 1997, NASA CR 4768.
- ⁷Weir, S. D., Jumper, J. S., Burley, C. L., and Golub, A. R., "Aircraft Noise Prediction Program Theoretical Manual: Rotorcraft System Noise Prediction System (ROTONET), Part 4," NASA TM 83199, April 1995.
- ⁸Brooks, T. F., Marcolini, M. A., and Pope, D. S., "Main Rotor Broadband Noise Study in the DNW," *Journal of the American Helicopter Society*, Vol. 34, No. 2, 1989, pp. 3–12.
- ⁹Zawodny, N. S., Boyd Jr., D. D., and Burley, C. L., "Acoustic Characterization and Prediction of Representative, Small-Scale Rotary-Wing Unmanned Aircraft System Components," 72nd American Helicopter Society Annual Forum, May 2016.
 - ¹⁰Brooks, T. F., Pope, D. S., and Marcolini, M. A., "Airfoil Self-Noise and Prediction," NASA RP 1218, 1989.
- ¹¹Burley, C. L. and Brooks, T. F., "Rotor Broadband Noise Prediction with Comparison to Model Data," *Journal of the American Helicopter Society*, Vol. 49, No. 1, January 2004, pp. 28–42.
- ¹²Zawodny, N. S. and Pettingill, N. A., "Acoustic Wind Tunnel Measurements of a Quadcopter in Hover and Forward Flight Conditions," 47th International Congress and Exposition on Noise Control Engineering, August 2018.
- ¹³Thurman, C. S., Zawodny, N. S., Pettingill, N. A., and Lopes, L. V., "Physics-informed Broadband Noise Source Identification and Prediction of an Ideally Twisted Rotor," AIAA SciTech Forum, No. January, 2021, pp. 1–10.
- ¹⁴Johnson, W., "A General Free Wake Geometry Calculation For Wings and Rotors," American Helicopter Society 51st Annual Forum, Fort Worth, Texas, 1995.